

# Study on Staged Start-up Mitigation Strategies for Water Hammer in Large-scale Centrifugal Pump Systems Based on One-dimensional and Three-dimensional Coupled Simulation

F. You and Q. Lan<sup>†</sup>

*School of Energy and Power Engineering, Lanzhou University of Technology, Lanzhou, 730050, China*

<sup>†</sup>Corresponding Author Email: [222085802095@lut.edu.cn](mailto:222085802095@lut.edu.cn)

## ABSTRACT

In large-scale centrifugal pump systems, the conventional linear start-up method often induces significant instantaneous pressure peaks (commonly referred to as water hammer) at the pump outlet when the valve is initially opened. These pressure surges not only exceed the system's designed operational pressure but also exert substantial mechanical stress on critical components, such as the impeller, potentially disrupting the system's stability and reliability. This study investigated whether a staged start-up method can effectively minimize the instantaneous pressure peaks generated at the pump outlet upon the completion of the start-up process. The transient external characteristics and internal flow field variations of a medium-to-high specific speed centrifugal pump system during staged start-up were investigated by integrating one-dimensional external characteristics analysis and three-dimensional internal flow field simulation. The study revealed that under the conventional linear start-up method, where the pump speed is increased to the rated speed before opening the valve, the pump-valve coordinated start-up mode generates an instantaneous pressure peak at the pump outlet, exceeding the designed head by 39%. In the staged start-up method, where the valve is opened in advance when the pump speed reaches 0.7 times the rated speed, the pressure peak is reduced by 23.94% compared with that in the linear start-up method. Additionally, the pressure fluctuation within the internal flow field is significantly mitigated, effectively ensuring the safe start-up and operation of the large-scale centrifugal pump.

## Article History

*Received October 10, 2024*

*Revised February 11, 2025*

*Accepted March 3, 2025*

*Available online May 5, 2025*

## Keywords:

*Large-scale centrifugal pump system*

*One-three dimensional simulation*

*Staged start-up*

*Pressure peak*

*Pressure fluctuation*

## 1. INTRODUCTION

In the field of hydraulic machinery, large-scale centrifugal pumps are widely used fluid machines with significant engineering value owing to their ability to transport large volumes of fluid efficiently and stably. As indispensable equipment in the industry, they play a critical role in numerous applications. However, during the start-up process of large-scale centrifugal pump systems, the combination of high flow rates and elevated base pressures results in pronounced water hammer effects. These sudden impacts can cause abnormal load shocks to the impeller and may even lead to pipe ruptures, thereby endangering the normal operation of the system. Therefore, investigating the start-up methods of large-scale centrifugal pumps is crucial for reducing pressure peaks during the start-up process, mitigating pressure fluctuations within the pump, and ensuring safe and stable operation of large-scale centrifugal pump systems.

The predominant methodology for analyzing the pump start-up process is the one-dimensional (1D) transient simulation approach. This method is characterized by its computational efficiency and structural simplicity, enabling a rapid yet coarse-grained assessment of transient hydraulic phenomena such as water hammer. By incorporating macro-scale parameters, including pump and valve openings as well as the time-dependent flow rate within the pipeline, this approach provides an expedient means to evaluate overall system performance. However, despite its computational expediency, the 1D method exhibits inherent limitations. It is constrained to global system parameters and lacks the spatial resolution necessary to capture localized pressure fluctuations, turbulence, and intricate flow dynamics within critical regions, such as the impeller, a pivotal internal component of the pump. Consequently, essential transient phenomena during start-up may be oversimplified or entirely overlooked, potentially leading

to an incomplete understanding of the underlying hydrodynamic behavior (Kan et al. 2020).

An alternative approach for achieving a more accurate simulation of the system start-up process is the implementation of a comprehensive three-dimensional (3D) system simulation. This full 3D computational methodology facilitates an in-depth analysis of flow field variations across the entire system during start-up, providing granular insights into the flow behavior of each component. Such detailed resolution is imperative for precisely evaluating pressure fluctuations and transient changes throughout the system. However, despite its enhanced accuracy, this approach presents significant challenges. It requires the meticulous modeling and numerical simulation of the three-dimensional geometry of all components within the pump system, including the water pipelines, valves, centrifugal pumps and associated elements. Consequently, this method becomes excessively complex, computationally prohibitive and highly sensitive to the initial boundary conditions at both the inlet and outlet, rendering it less practical for certain large centrifugal pump systems.

Therefore, the 1D calculation approach for simulating the pump system start-up process is inherently limited in its ability to capture detailed internal flow characteristics. In contrast, full 3D simulations, while offering more accurate representations of flow dynamics, are computationally intensive, particularly for large centrifugal pump systems. Recently, there has been a growing shift towards employing a coupled 1D–3D simulation method, which combines the strengths of both approaches. This hybrid methodology harnesses the complementary advantages of 1D and 3D simulations, 1D calculations are utilized to evaluate the overall flow dynamics of large centrifugal pump systems, while 3D simulations focus on resolving the localized flow characteristics in complex regions within the pump. By retaining the computational efficiency of 1D analysis and mitigating the computational burden of full 3D simulations, this approach strikes a balance between accuracy and computational feasibility. It enables a precise assessment of overall pump performance during start-up, while simultaneously capturing the complex internal flow dynamics and the concomitant changes occurring both within the pump and across the system during various stages of the start-up process (Fu et al., 2021). Existing studies on the coupling of 1D and 3D phases in centrifugal pump start-up processes includes that of Yun et al. (2020), who analyzed the characteristics of the pump and the evolution of the internal flow field during the transition stage of a multistage centrifugal pump with the valve both off and on. That study found that a multistage centrifugal pump with the valve open produced more stall regions in the rotating channel during the initial transition process. Li et al. (2020) investigated the external transient hydrodynamic performance of pumps and the internal flow during transient start-up, thereby providing valuable insights for predicting the performance of the pump and valve during the start-up process. Li et al. (2021b) established a complete three-dimensional closed-loop model to numerically simulate the start-up process of a mixed-flow pump. The simulation

provided all the relevant parameters during start-up, revealing a trend of increase followed by a decrease over time. Simultaneously, Li et al. (2021a) established a measurement system for transient external characteristics and pressure pulsations during the start-up process of a mixed-flow pump, and found that the flow and head curves can be categorized into three stages as the pump speed increases: slow rise, rapid rise, and subsequent stabilization. Xu et al. (2021) conducted a numerical simulation of the three-dimensional transition process during the start-up of a full overflow system of an axial-extension cross-flow pump. The results indicated that the pump head initially increased and then decreased to the rated head during the start-up process. Additionally, the pressure distribution gradient in the impeller section was influenced by changes in the start-up speed and flow rate of the pump. Zhang et al. (2021) numerically analyzed the start-up process of axial water jet propellers, focusing on the effects of the start-up time and transient characteristics of the waterline height. These results indicate that shorter start-up times for water-jet propellers lead to increased levels of hysteresis. Tanaka et al. (2021) conducted an experimental and computational fluid dynamics (CFD) study on the transient behavior of a fast-start centrifugal pump. By comparing the experimental results with the CFD simulations, it was concluded that the transient characteristics deviated from those at the quasi-steady state owing to delays in the formation of the flow field within the pump during the transient phase compared with the steady-state flow field. Lu et al. (2022) established a transient performance prediction model for the start-up process of mixed-flow pumps and constructed a three-dimensional geometric model of a mixed-flow pump and piping system. The results indicate that the flow rate during the start-up process lags behind the increase in speed, initially growing slowly before ultimately stabilizing at the end of the speed-acceleration phase. Desheng et al. (2022) investigated the effect of the number of blades on the cavitation flow during start-up by conducting a transient cavitation simulation study. Li et al. (2022) conducted a numerical analysis of the transient flow field in a prefabricated pumping station with two identical pumps, and examined the interference between adjacent components and the external characteristics of the pumps. The analysis revealed that the increase in pump head occurred in two stages: first, it lagged behind the increase in impeller speed, followed by a rapid increase in pump head. Zhang et al. (2022) conducted transient experiments at two valve openings and four rotational speeds using a PAT test rig. The results revealed that hydrostatic shock was prevalent at the outlet of the PAT and exhibited hysteresis and weakening as the stabilized rotational speed increased. Ding et al. (2023) proposed a specialized impeller with modifications to the vane pressure surface to mitigate the strong pressure pulsations during the start-up of centrifugal pumps. Tang et al. (2023) analyzed the changes in the external characteristic parameters, pressure fluctuations, and shaft vibration data during the pump start-up process using a multichannel synchronous signal acquisition system. The analysis revealed a positive correlation between the amplitude of shaft vibration during start-up and the acceleration of the impeller. Xia et al. (2024) utilized Flowmaster software to

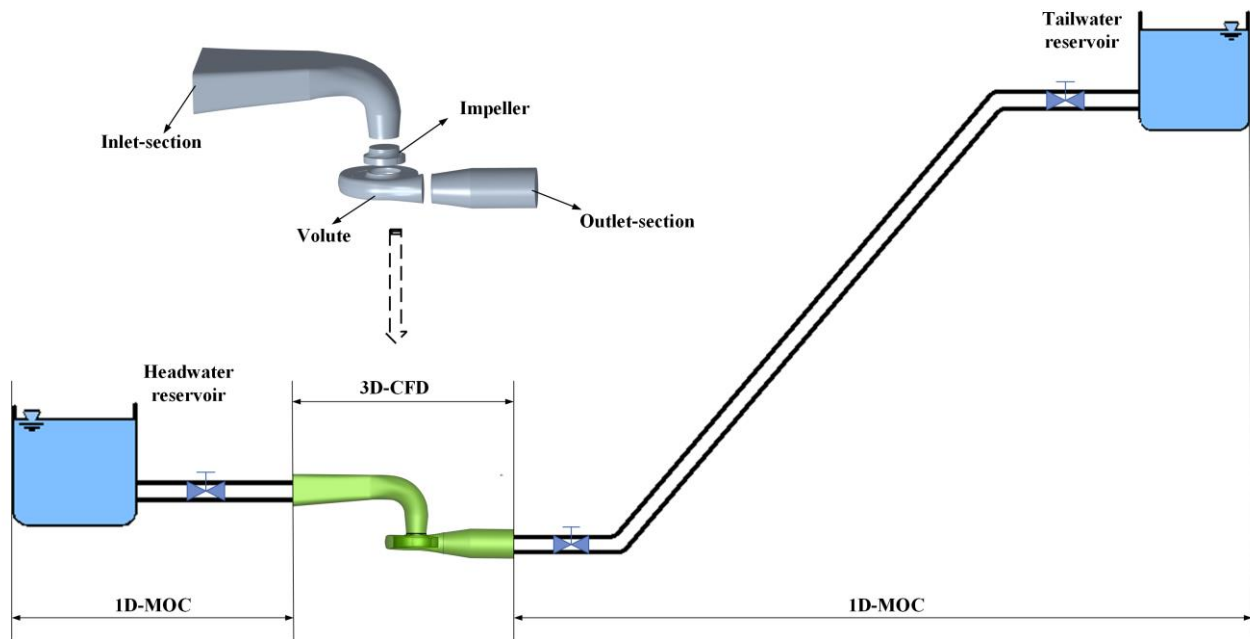


**Fig. 1 Schematic of the coupled simulation for the centrifugal pump system**

obtain the speed and flow characteristic curves of a pump under different valve openings to study the transient characteristics of a multistage pump during start-up. The results indicated that the time required for the flow to reach a steady state at the beginning of the start-up period lagged significantly behind the time needed for the speed to stabilize. Additionally, the evolution of the internal flow field of the pump under transient conditions lagged behind that observed under quasi-steady-state conditions. Liu et al. (2024b) provided an in-depth analysis of the start-up and shutdown transient processes of a high-flow, high-power centrifugal pump, exploring the trends in the pressure pulsation mixing amplitudes during these transient phases. Zhang et al. (2024) established an operational model of a centrifugal pump system and employed a combination of Flowmaster and CFX software to analyze the effects of acceleration time and mode on the performance of the variable-speed control process and the internal flow field of the centrifugal pump. The analysis revealed significant variations in the turbulence kinetic energy within the pump, with high turbulence kinetic energy and vorticity widely distributed, indicating pronounced transient effects.

Current research on mitigating the water hammer effect during the pump start-up process predominantly concentrates on linear pump start-up and the regulation of pressure peak phenomena through controlled valve opening and closing. However, fewer studies have investigated the staged start-up process of centrifugal pumps, where both the pump and valve openings are incrementally adjusted to alleviate the pressure peaks typically associated with linear start-up. Research on the simultaneous evolution of 1D and 3D transient characteristics of both the internal and external flow fields in this staged start-up mode remains relatively scarce. Consequently, our research focus has shifted towards the development of a staged start centrifugal pump system,

utilizing coupled 1D-3D simulations to comprehensively assess the dynamic behavior of the system, used the external characteristic results obtained from the one-dimensional method (Shi et al. 2023) as the boundary conditions for the three-dimensional simulation. The internal and external flow fields during the staged start-up process were simulated to reveal the effects of the interaction between the internal and external flow fields on the pressure peaks and fluctuations in both the linear and staged start-up modes. The aim was to provide a theoretical basis for the effective reduction of pressure peaks and fluctuations during the start-up process of large-scale centrifugal pumps through the coordination of the internal and external flow fields in the staged start-up method.

## 2. PHYSICAL MODEL AND NUMERICAL CALCULATION METHODS

### 2.1 Geometric Model and Mesh Generation

This study employs a combined one- and three-dimensional simulation method to study the changes in the internal and external characteristics during the start-up process of a medium- to high-specific-speed centrifugal pump pipeline system. In particular, a three-dimensional numerical simulation method was used to accurately simulate the computational domain of the centrifugal pump, including the inlet section, impeller, volute, and outlet section. To explore the internal flow behavior during the start-up process and ensure the accuracy of the piping system simulation, a one-dimensional characteristic line method was employed to calculate the transient external characteristics of the piping system. The computational domain of the piping system for this joint simulation is illustrated in Fig. 1. The specific parameters of the one-dimensional calculation model were as follows. The water levels in the inlet and outlet reservoirs were set

**Table 1 Centrifugal pump model parameters and grid independence validation scheme**

Centrifugal pump parameters	Numerical	Mesh scheme	Quantity	Head
Pump Inlet Equivalent Diameter $D_1$ /mm	2850	1	1251550	57.31
Pump Outlet Diameter $D_2$ /mm	1900	2	1650192	57.67
Flow Rate $Q$ /m <sup>3</sup> s <sup>-1</sup>	8	3	1965392	57.87
Head $H$ /m	56	4	2336224	58.54
Rotational Speed $N$ /rpm	375	5	2688543	58.67
Number of Blades $Z$	6	6	3634127	58.60
Specific Speed $n_s$	189	7	5006181	58.66

to 2 m. The performance parameters of the pump are consistent with those listed in Table 1, and the energy losses in the system were considered. The elevation of the water transport pipeline was 53.8 m, and the pump operated at a design head of 56 m. The specific parameters of the centrifugal pump are listed in Table 1.

The three-dimensional simulation employs an unstructured polyhedral mesh to discretize the computational domain of the centrifugal pump, as illustrated in Fig. 2. To enhance calculation accuracy, the head region of the impeller blade was refined. In addition, a boundary layer was implemented at the wall, which comprised five layers. The first layer had an aspect ratio of 10, the fifth layer had an aspect ratio of 5, and the mesh growth rate was set to 1.2. The  $Y^+$  value on the impeller blade surface remained below 30, ensuring suitability for turbulence modeling using the SST  $k-\omega$  model (Wang et al. 2024) approach, with a mesh size of 3.63 million. The head fluctuation was found to be less than 0.15% in Feng et al. (2020); therefore, mesh scheme 6 was selected for the simulation, resulting in a total of 3,634,127 polyhedral elements in the computational domain. The grid independence validation and head comparison results are presented in Table 1.

### 2.2 Boundary Conditions and Turbulence Modeling

In contrast to the traditional simultaneous one- and three-dimensional coupling method, this study first calculated the pump outlet pressure and flow rate in a one-dimensional pipeline under different start-up modes, obtaining the time-varying curves of outlet pressure and flow rate. Subsequently, the curve was sampled at fixed time intervals to determine the pressure and flow rate at each sampling point, forming a dataset comprising time, pressure, and flow rate values. The sampled datasets were then converted into a format recognizable by the numerical simulation software and applied as boundary conditions at the pump inlet and outlet in the three-dimensional simulation for computational analysis. This approach replaces the entire transient computational process with a quasi-steady-state process at discrete time intervals, thereby achieving a combined one- and three-dimensional simulation.

3D numerical simulations were conducted using ANSYS Fluent 2019, the SST  $k-\omega$  turbulence model was employed in the three-dimensional simulation, utilizing the SIMPLER algorithm for numerical computation.

The pump inlet boundary condition was set as a pressure inlet, whereas the outlet boundary condition was

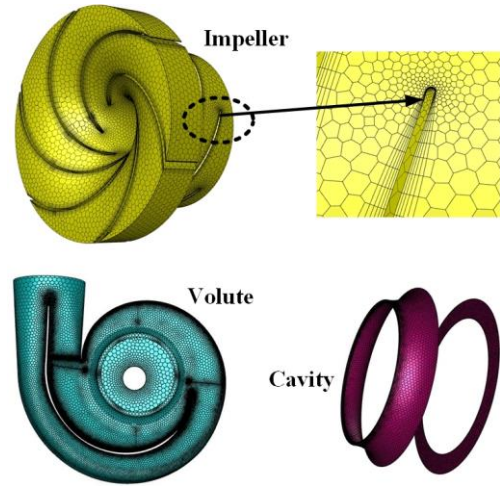


**Fig. 2 Computational domain mesh for the centrifugal pump**

defined as a mass flow outlet (Liu et al. 2024a). A no-slip wall boundary condition was applied, with the computational convergence accuracy established at  $10^{-5}$ . The transient calculation employed a time step of  $3^\circ$  of impeller rotation for each calculation moment, resulting in  $\Delta t = 0.001333s$  at the rated speed. The number of iterations was set to 100 for each time step, and data analysis was performed on the last three revolutions of stable pump operation.

The continuity and momentum equations used in the numerical calculations are as follows:

$$\frac{\partial \rho}{\partial t} + \nabla \cdot (\rho \bar{\mathbf{u}}) = 0 \quad (1)$$

$$\frac{\partial (\rho u)}{\partial t} + \nabla \cdot (\rho u \mathbf{u}) = \nabla \cdot (\mu \nabla u) - \frac{\partial \rho}{\partial x} + S_u \quad (2)$$

$$\frac{\partial (\rho v)}{\partial t} + \nabla \cdot (\rho v \mathbf{v}) = \nabla \cdot (\mu \nabla v) - \frac{\partial \rho}{\partial y} + S_v \quad (3)$$

$$\frac{\partial (\rho w)}{\partial t} + \nabla \cdot (\rho w \mathbf{w}) = \nabla \cdot (\mu \nabla w) - \frac{\partial \rho}{\partial z} + S_w \quad (4)$$

where  $\rho$  is the fluid density,  $\mathbf{u}$  represents the velocity components,  $\mu$  denotes the fluid viscosity,  $\nabla$  is the gradient operator, and  $\nabla \cdot$  is the divergence operator.  $S_u$ ,  $S_v$ ,  $S_w$  denote the source terms.

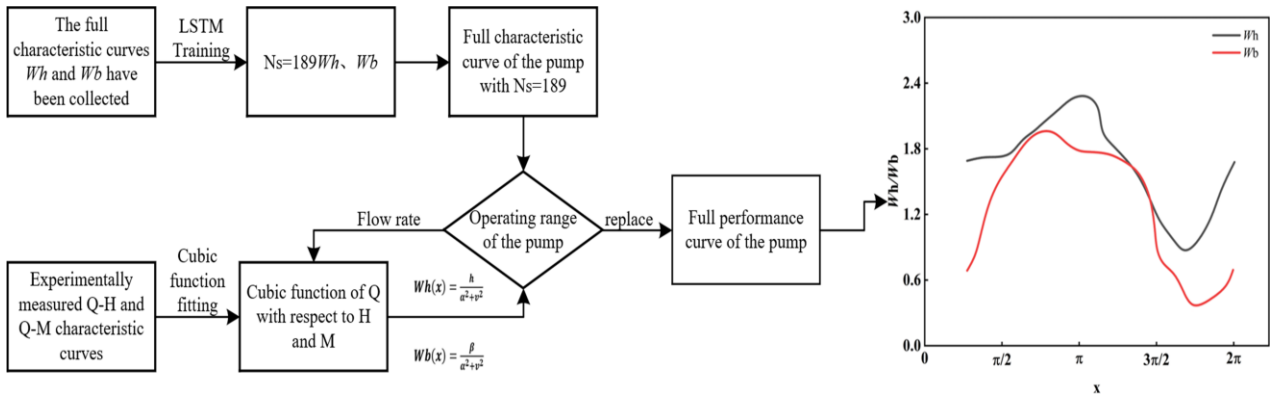


**Fig. 3 Full characteristic curve of the centrifugal pump**

The turbulence model SST  $k-\omega$  introduces turbulent kinetic energy  $k$  and specific dissipation rate  $\omega$  to close the system of equations. The main equations are as follows.

The equation for turbulent kinetic energy  $k$  is given by

$$\frac{\partial(\rho k)}{\partial t} + \frac{\partial(\rho k u_i)}{\partial x_i} = P_k - \beta^* \rho k \omega + \frac{\partial}{\partial x_i} \left[ (\mu + \delta_k \mu_t) \frac{\partial k}{\partial x_i} \right] \quad (5)$$

In the equation,  $P_k$  is the production term of turbulent kinetic energy caused by shear stress,  $\beta^*$  is a model coefficient with a value of 0.09,  $\omega$  is the specific dissipation rate,  $\mu_t$  is the turbulent viscosity, and  $\sigma_k$  is the Prandtl number with a value of 1.0.

The specific dissipation rate  $\omega$  is

$$\frac{\partial(\rho \omega)}{\partial t} + \frac{\partial(\rho \omega u_i)}{\partial x_i} = \alpha \frac{\omega}{k} P_k - \beta \rho \omega^2 + \frac{\partial}{\partial x_i} \left[ (\mu + \delta_\omega \mu_t) \frac{\partial \omega}{\partial x_i} \right] + 2(1 - F_1) \rho \sigma_{\omega 2} \frac{1}{\omega} \frac{\partial k}{\partial x_i} \frac{\partial \omega}{\partial x_i} \quad (6)$$

In the equation,  $\beta$  and  $\sigma_\omega$  are empirical constants, with values of 0.075 and 0.5, respectively.  $F_1$  is a blending function used to switch between the  $k-\omega$  and  $k-\epsilon$  models in different regions.

### 2.3 Correction of the Full Characteristic Curve of the Centrifugal Pump

The full characteristic curve of the pump is indispensable in one-dimensional calculations (Gu, 2021). By providing the complete characteristic curve, the transient parameter variations during the unit start-up process can be calculated, which helps determine the boundary conditions for subsequent simulations. To determine accurate boundary conditions, the LSTM algorithm was used to train the full characteristic curves for the rotational speed range of  $n_s = 57.3-952.65$ ; thus, the full characteristic curve of the pump with a specific speed of  $n_s = 189$  was obtained in this study. Simultaneously, the experimentally measured pump flow-

head and flow-torque characteristic curves were fitted, yielding cubic polynomial fitting formulas for any given flow rate, head, and torque, as shown in Eqs. (7) and (8). By substituting the flow rates from the pump operating condition region into the cubic polynomial fitting equations derived from the LSTM-trained characteristic curves, the corresponding head and torque values were obtained. These values were subsequently incorporated into the relevant equations (Wang et al., 2017) to generate the pump operating condition region curve, which was subsequently integrated back into the LSTM curves to produce a complete characteristic curve. The replacement process and the resulting pump characteristic curves are shown in Fig. 3.

$$H = 57.6363 + 2.2129Q_i - 0.1825Q_i^2 - 0.0113Q_i^3 \quad (7)$$

$$M = -134462.41 + 19450.67Q_i - 3617.79Q_i^2 + 164.30Q_i^3 \quad (8)$$

In Eqs. (7) and (8),  $Q_i$  represents the flow variation on any characteristic curve, and  $H$  and  $M$  denote the corresponding head and torque at any given flow rate  $Q_i$ , respectively. The correlation coefficients for the two fitted curves were 0.9986 and 0.9994, indicating a high degree of correlation in the fitting, thus ensuring that the predictions met the requirements of the actual data.

### 2.4 Experimental and Computational Method Validation

The circulation system used in this experiment is shown in Fig. 4. This system is a closed-loop testing platform that includes a reservoir, electromagnetic flowmeter, pressure tank, model unit, tailwater tank, stainless-steel piping system, and weighing bucket. The experiment was conducted in an open-loop configuration, with the test rig equipped with high-precision flow meters, differential pressure sensors, absolute pressure sensors torque sensors. The measurement accuracy and operational stability of all parameters in the test rig met the requirements of the GB and IBC standards, with a power rating of 300 kW and a maximum speed of 3000 rpm. An electromagnetic flowmeter (model T8705TSE) was installed in the measuring pipeline to monitor the flow rate.

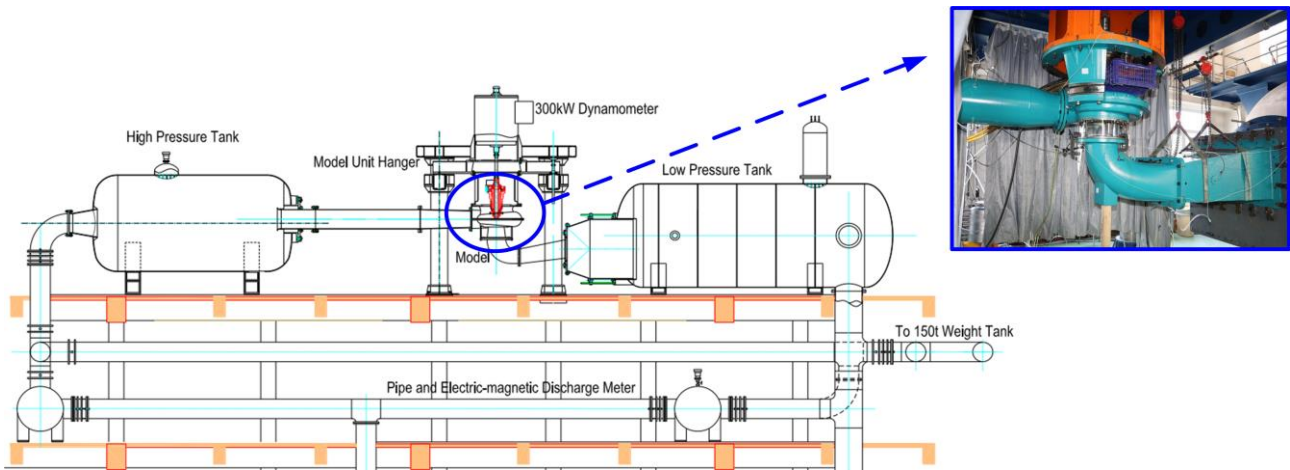


**Fig. 4 Centrifugal pump testing apparatus**

Eight operating conditions under normal pump operation were selected for experimental testing and numerical simulation analysis for validation. A comparison between the simulation results and experimental results for each operating condition is shown in Fig. 5. The experimental flow-head and flow-efficiency characteristic curves exhibited the same trend as the numerical simulation curves. The maximum deviation between the experimental head and the simulated head was observed at  $1.2Q_d$  ( $Q = 9.5 \text{ m}^3/\text{s}$ ), with a maximum error of 4.44%; the maximum deviation between the experimental efficiency and the simulated efficiency occurred at  $0.65Q_d$  ( $Q = 5.5 \text{ m}^3/\text{s}$ ), with a maximum error of 4.02%. The error between the head and efficiency under all simulated operating conditions did not exceed 5% (Lin et al., 2021). It is concluded that the numerical simulation is feasible within the acceptable error range.

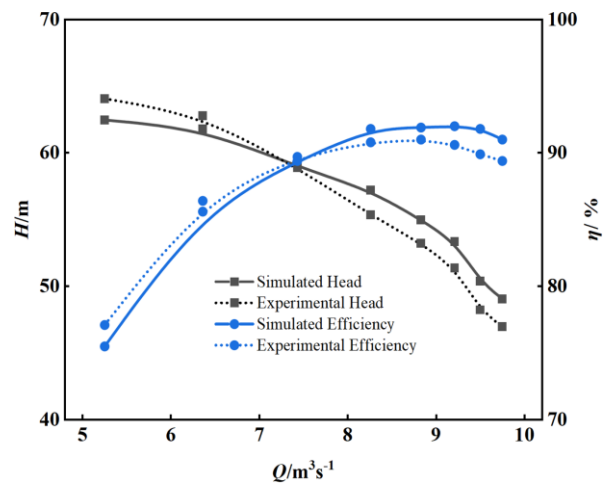


**Fig. 5 Comparison between numerical simulation and experimental results**

### 3. RESULT AND ANALYSIS

#### 3.1 Impact of Different Start-up Methods on the External Characteristics of Large-scale Centrifugal Pump Systems

During the start-up process of large-scale centrifugal pump systems, the combination of high flow rates and elevated base pressures results in significantly larger baseline axial and radial forces. This leads to pronounced water-hammer effects that threaten the normal operation of the system. Consequently, studying the water hammer phenomenon during the start-up process of large-scale centrifugal pump systems is more critical than that of smaller pumps. Therefore, this study investigated whether the staged start-up method could effectively mitigate this phenomenon by designing multiple sets of linear and staged start-up schemes. This study focused on analyzing the variation patterns of the external characteristics of the system.

#### 3.2 Comparison of External Characteristics Under Different Start-up Methods

The variations in the pump outlet pressure and flow rate during the linear and staged start-up processes are listed in Table 2.

The variations in the external characteristic parameters under different start-up methods, as listed in Table 2, are illustrated in Fig. 6. Figure 6a shows the variation in the pressure peak values with the linear valve opening time, and the influence of the valve opening time on the pressure peak values can be categorized into two types. In Scheme 1, under the linear start-up method, when the pump speed reaches the rated speed and the valve is opened, the valve opening time does not affect the pressure peak value, which remains at 77.71 m. Scheme 2 and Scheme 3 show that under the staged start-up method, when the pump speed has not yet reached the rated speed and the valve is opened in advance, the pressure peak value increases as the valve opening time is extended.

Figure 6b shows the variation in the pressure peak duration with the length of the linear valve opening time, which indicates that the length of the valve opening time affects the duration of the pressure peak. Under both the linear and staged start-up methods, in Schemes 1, 2, and 3, the duration of the pressure peak increased with the extension of the valve opening time. In all three schemes, the duration of the high-pressure zone was the longest when the valve opening time reached 20 s. The pressure

**Table 2 Start-up Schemes and Corresponding Variations in External Characteristic Parameters**

Start-up type	Starting scheme	Starting period/s	Valve opening period/s	Pump stable operation period/s	Pressure peak value/m	Duration of pressure peak value/s
Linear start-up	Option 1	0-7.5	7.5-12.5	7.5-7.5	77.71	4.5
			7.5-17.5		77.71	7.5
			7.5-22.5		77.71	10.5
			7.5-27.5		77.71	14
Staged start-up	Option 2	0-7.5	5-10	7.5-7.5	59.11	3
			5-15		64.46	4.5
			5-20		66.58	7.5
			5-25		67.51	11.5
Staged start-up	Option 3	0-7.5	5-10	5-6	56.58	0
				5-7	56.14	0
				5-8	56.04	0
				5-9	56.04	0
				5-10	56.04	0
			5-15	5-6	62.10	3.5
				5-7	56.43	2.5
				5-8	55.99	1.5
				5-9	55.98	0
				5-10	55.98	0
			5-20	5-6	64.88	7
				5-7	56.85	5.5
				5-8	55.98	4.5
				5-9	55.95	3.5
				5-10	55.95	2.5
			5-25	5-6	66.38	10
				5-7	57.17	9.5
				5-8	55.98	8
				5-9	55.93	7
				5-10	55.93	6

**Table 3 Start-up Modes in Combined Simulation**

Start-up type	Starting scheme	Starting period/s	Valve opening period/s	Pump stable operation period/s
Linear start-up	Mode 1	0-7.5	7.5-12.5	7.5-7.5
Staged start-up	Mode 2	0-7.5	5-10	7.5-7.5
Staged start-up	Mode 3	0-7.5	5-10	5-10

peak durations in Schemes 1, 2, and 3 were 14, 11.5, and 10 s, respectively.

Figure 6c shows the relationship between the steady pump operation time and the valve opening time. The figure shows that during the staged start-up, when the valve is opened before the pump reaches the rated speed, the shorter the steady operation time of the pump, the larger is the pressure peak. For the same valve-opening duration, the pressure peak decreased as the steady operation time of the pump increased.

**3.3 Verification of One-Dimensional and Three-Dimensional Combined Simulation during the Start-up Process and One-Dimensional Characteristic Analysis**

To further investigate the internal flow characteristics during the pump start-up process, three modes were selected from the start-up schemes listed in Table 2. A

combined simulation approach was employed to study their specific external and internal flow characteristics.

As listed in Table 3, the total start-up duration for these three modes is 7.5 s, with a total valve-opening duration of 5 s. The modes are as follows. Linear start-up Mode 1: the pump reaches its rated speed within 7.5 s, and the valve is opened at this moment, achieving full linear opening between 7.5 and 12.5 s. Staged start-up Mode 2: the pump reaches its rated speed within 7.5 s, but the valve is opened in advance at 0.7 times the rated speed. The valve begins to open fully linearly from 5 to 10 s. Staged start-up Mode 3: the pump accelerates to 0.7 times the rated speed within 5 s and operates at this speed for 5 s. It then resumes acceleration to the rated speed at 12.5 s in the same manner as in the first phase, while the valve fully opens linearly from 5 to 10 s. The three start-up modes are illustrated in Fig. 7a.

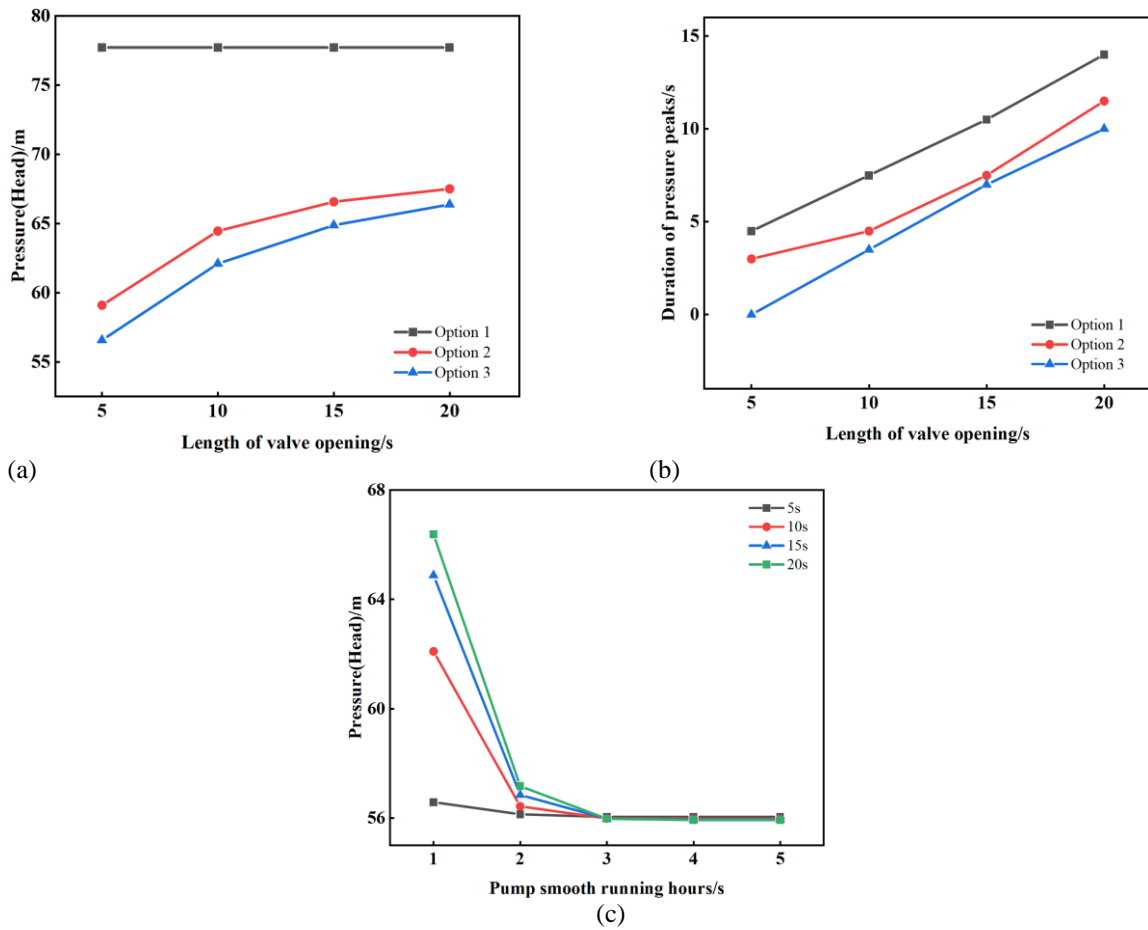


Fig. 6 Relationship between valve opening time, pressure, and pressure peaks

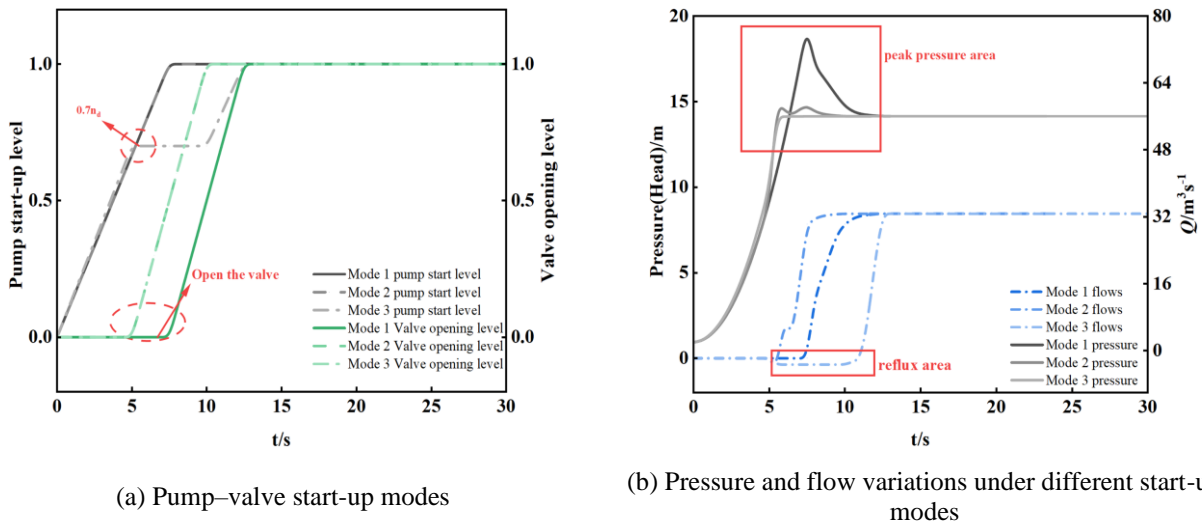
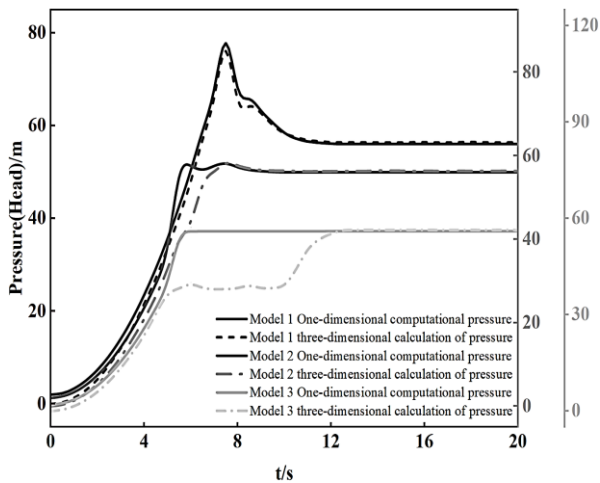


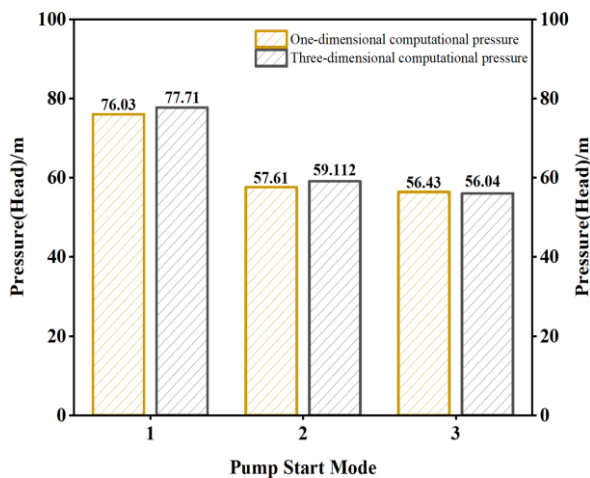
Fig. 7 Pump start-up modes and variations in flow and pressure

Figure 7b illustrates the variations in pressure and flow rates for the three start-up modes. The trends of the pressure and flow rate variations in the figure are generally consistent across the three modes. However, the magnitude of the pressure peaks varies owing to differences in the rate of pump speed increase and the duration of valve opening. In Mode 1, when the valve was opened at 7.5 s, the pump pressure peak reached 77.71 m, which exceeded the normal design head of the pump by

39%. In Mode 2, at 5.5 s, the pressure peak dropped to 59.11 m, exceeding the normal design head of the pump by 5.5%. In Mode 3, at 5.5 s, the pressure peak decreased to 56.04 m. In Mode 1, when the pump speed reached the rated speed and the valve was opened, the pressure peak occurred at the moment the valve was activated. In Modes 2 and 3, when the valve was opened in advance at 0.7 times the rated pump speed, the pressure peak was observed 0.5 s after the valve activation. The pump outlet



(a) Comparison of pressure curves under one- and three-dimensional coupled simulations



(b) Comparison of pressure peaks under one- and three-dimensional coupled simulations

**Fig. 8 Validation of one- and three-dimensional coupled simulations**

also exhibited backflow phenomena under the different pump start-up modes. In all three modes, the flow rate within the pump gradually increased after the valve was opened, eventually reaching the rated flow rate after the valve was closed. Among the three modes, only Mode 3 exhibited backflow when the pump speed remained constant. The duration of constant speed was 5 s, during which backflow occurred for 6 s, with a maximum backflow rate of 0.37 m<sup>3</sup>/s, representing 4.63% of the system's rated flow rate.

The comparison of the variation curves of the external characteristics, including pressure and flow rate, under the three pump-starting modes reveals significant differences. It can be concluded that opening the valve in advance when the pump speed reaches 0.7 times the rated speed effectively reduces the pressure peak at the pump outlet without causing backflow, which is considered the optimal scheme for the three operational modes.

To further investigate the transient internal flow characteristics in these three pump-starting modes, we first validated the feasibility of the one- and three-

dimensional joint simulation approaches. Specifically, we compared the one-dimensional calculated pressure with the three-dimensional simulated starting pressure for the three pump starting modes, as shown in Fig. 8.

As shown in Fig. 8a, the pressure curves from the one- and three-dimensional coupled simulations were largely consistent. In the figure, there is a deviation in the pressure curve of Mode 3 during the interval from 5.5 to 11 s. This deviation is primarily due to the pump entering a steady operating phase at 5 s, during which the valve is opened. This resulted in backflow at the pump outlet, causing the pump to deviate from its normal operating conditions between 5.5 and 11 s. Consequently, the pump enters a braking condition, and an abnormal operating state leads to an inability to achieve the expected pressure during this phase.

As shown in Fig. 8b, the deviations in the pressure peaks between the one-dimensional calculation and three-dimensional simulation did not exceed 3%, 2.6%, and 0.7% of the designed head, respectively. This indicates that the combined one- and three-dimensional simulation method used in this study is effective for describing the transient characteristics during the pump start-up process.

### 3.4 Comparison of Internal Flow Characteristics under Three Start-up Methods

Significant pressure peaks were observed in Modes 2 and 3 at 5.5 s, whereas a pressure peak was noted in Mode 1 at 7.5 s. Therefore, the study focused on the transient flow field variations at four time points during the starting process of the pump: 5.5, 6.5, 7.5, and 8.5 s.

### 3.5 Analysis of Pressure, Velocity, and Turbulent Kinetic Energy under Three Pump Starting Modes

Figure 9 shows the pressure variation contours at the midsection of the impeller for the three pump-starting modes at four specific starting times.

The static pressure distribution patterns at the midsection of the impeller are similar across the three modes, showing a trend of low pressure at the impeller inlet and high pressure at the impeller outlet. At 5.5 s, a localized high-pressure region is observed at the impeller outlet position in all three modes. In Mode 1, the distribution is more pronounced, whereas Modes 2 and 3 show a less varied distribution. This occurs primarily because the pump outlet valve is not yet open in Mode 1, whereas the valve in Modes 2 and 3 has just been opened. At 6.5 s, the localized high-pressure regions in the impeller gradually diffused into the flow channel across all modes. In Modes 1 and 2, the extent of the localized high-pressure regions was broader than the distribution observed at 5.5 s. The pressure within the impeller gradually increased as the rotational speed rose. At this moment, the valve in Mode 1 remained closed, whereas in Modes 2 and 3, the opening of the valve at this moment led to a significant difference between the high-pressure and low-pressure areas within the impeller flow channel. At 7.5 s, the pressure within the impeller reached its maximum value across all time points for each mode, and a localized high-pressure region was still present at the

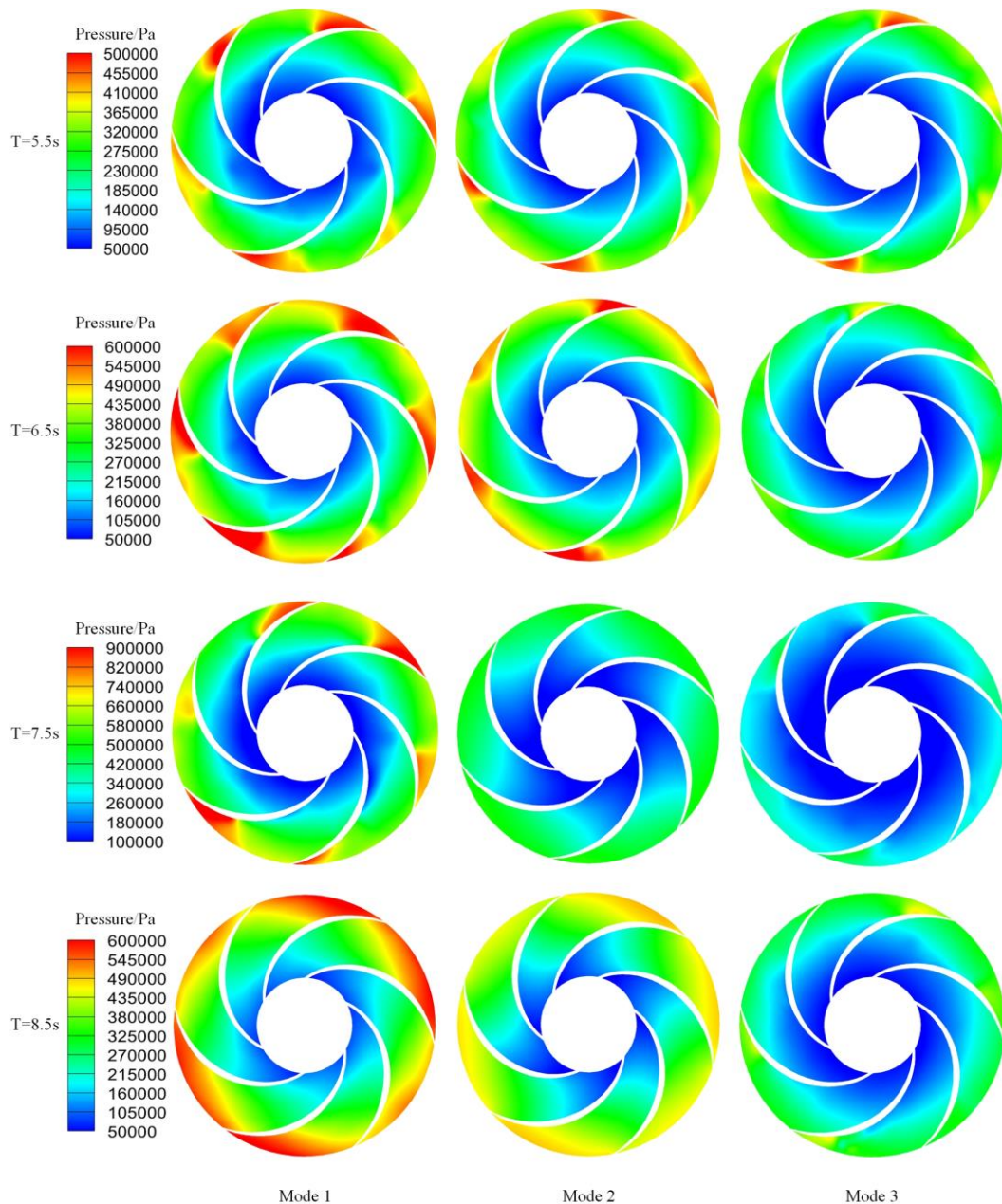


**Fig. 9 Pressure distribution at the mid-section of the impeller under different pump starting modes**

impeller outlet position in Mode 1. In Modes 2 and 3, the pressure gradient was relatively uniform. This was primarily due to the rapid pressure changes within the impeller in Mode 1 as the valve was initially opened, whereas in Modes 2 and 3, the valve had been opened to  $0.5^\circ$ , resulting in no significant pressure fluctuations. Simultaneously, this internal characteristic change led to a peak in the external characteristic pressure for Mode 1 at this moment. At 8.5 s, the pressure within the impeller gradually decreased across all modes, and the pressure gradient remained unevenly distributed in Mode 1. In comparison, the pressure gradient variation in Mode 2 was the most uniform across all time points. At 7.5 s, when the pump reached its rated speed, there were no noticeable pressure gradient fluctuations within the impeller. The starting method effectively alleviated the pressure fluctuations when the pump reached its rated speed. This internal characteristic was precisely what led to the

observed reduction in the pressure peak of the curve for Mode 2 in the one-dimensional external characteristics.

Figure 10 shows the variation in the velocity field at the midsection of the impeller for the three pump-starting modes at different time points.

In each mode, the velocity gradually increased from the impeller inlet to the impeller outlet. From 5.5 to 7.5 s, in Mode 1, the high-velocity region at the mid-position of the impeller working surface diffused into the flow channel. In Mode 2, the high-velocity region in the rear half of the impeller working surface gradually diminished as it diffused into the flow channel. In Mode 3, the high-velocity regions within the flow channel were distributed in clusters along the blade working surface. At 7.5 s, the valve in Mode 1 was opened, and the overall flow velocity within the impeller was at its highest, whereas in Modes 2 and 3, the valve had already been opened to  $0.5^\circ$ , resulting

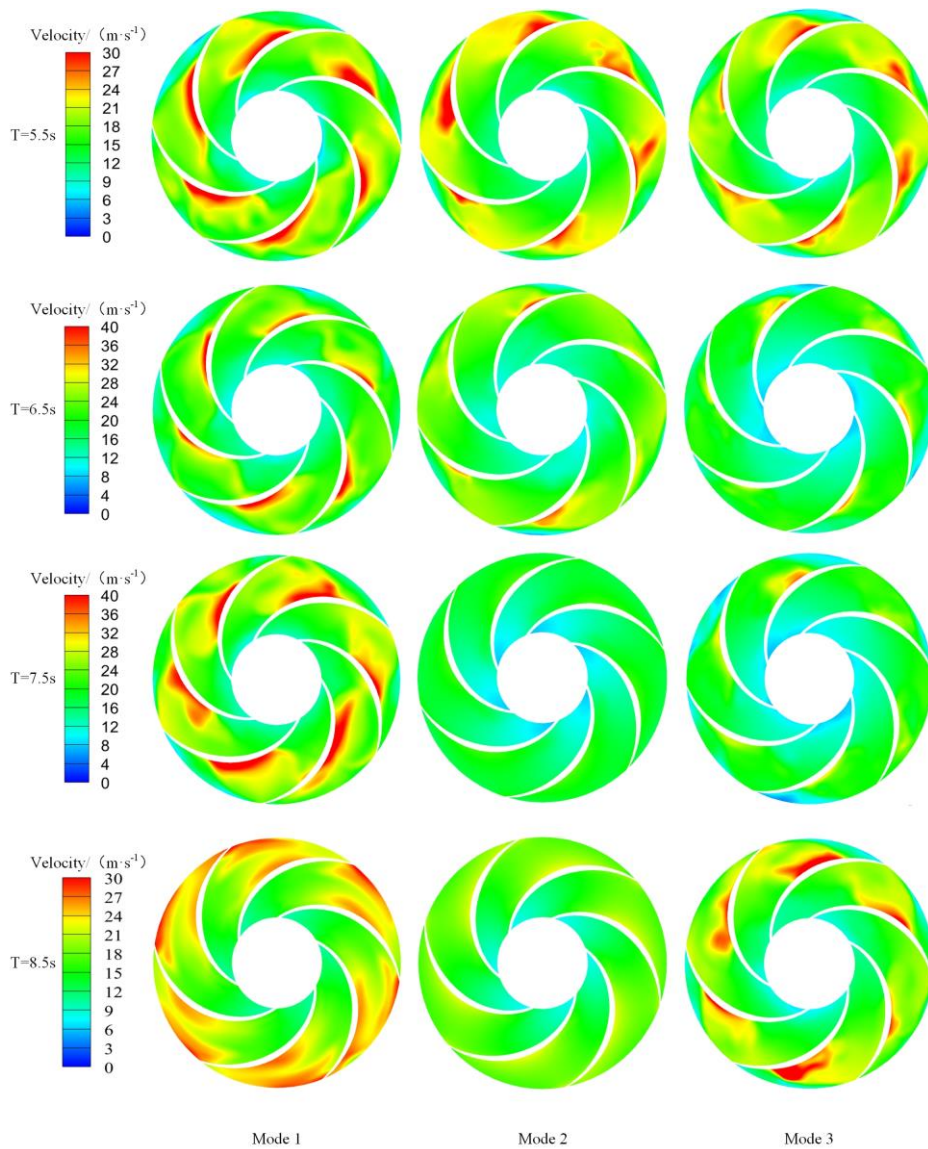


**Fig. 10 Velocity distribution at the mid-section of the impeller under different pump starting modes**

in a smaller change in the velocity gradient within the impeller compared with that at the previous time point. At 8.5 s, the velocity within the flow channel gradually decreased across all modes. At this time, the high-velocity region in Mode 1 gradually concentrated at the impeller outlet as time progressed. In Mode 2, the flow velocity within the impeller channel gradually became evenly distributed over time. In Mode 3, there were some high-velocity regions present on the back surface of the impeller. In the velocity field, Mode 2 exhibited a more uniform velocity gradient than the other two modes, and this internal flow characteristic corresponded to the pressure variation.

Figure 11 shows the turbulent kinetic energy distribution at the midsection of the impeller for the three pump-starting modes at different time points.

Different pump-starting modes and valve-opening methods influence the distribution of turbulent kinetic energy within the impeller. At 5.5 and 6.5 s, as the pump speed gradually increased, the turbulent kinetic energy within the impeller became more intense. In Modes 1 and

3, the turbulent kinetic energy was more widely distributed. In Mode 2, a small amount of turbulent kinetic energy was distributed at the pressure side of the impeller outlet, because the valve had already opened at 5.5 s. As the pump reached its rated speed, the flow within the impeller gradually adapted to the valve opening, resulting in a lower distribution of turbulent kinetic energy. At 7.5 s, the turbulent kinetic energy was most pronounced. In Mode 1, the turbulent kinetic energy was distributed across the impeller working surface and throughout the flow channel near the outlet, whereas in Mode 2, the distribution of turbulent kinetic energy was minimal. This occurred because at this moment, the valve in Mode 1 had just opened, causing rapid changes in velocity and flow within the impeller, leading to significant fluctuations in turbulent kinetic energy. In Modes 2 and 3, the valve opening allowed the impeller to adapt to the changes in pressure and flow, resulting in a more uniform distribution of turbulent kinetic energy. At 8.5 s, the valves in all modes were fully opened, and the distribution of the turbulent kinetic energy was the most uniform in Mode 2, whereas Modes 1 and 3 exhibited some areas of uneven

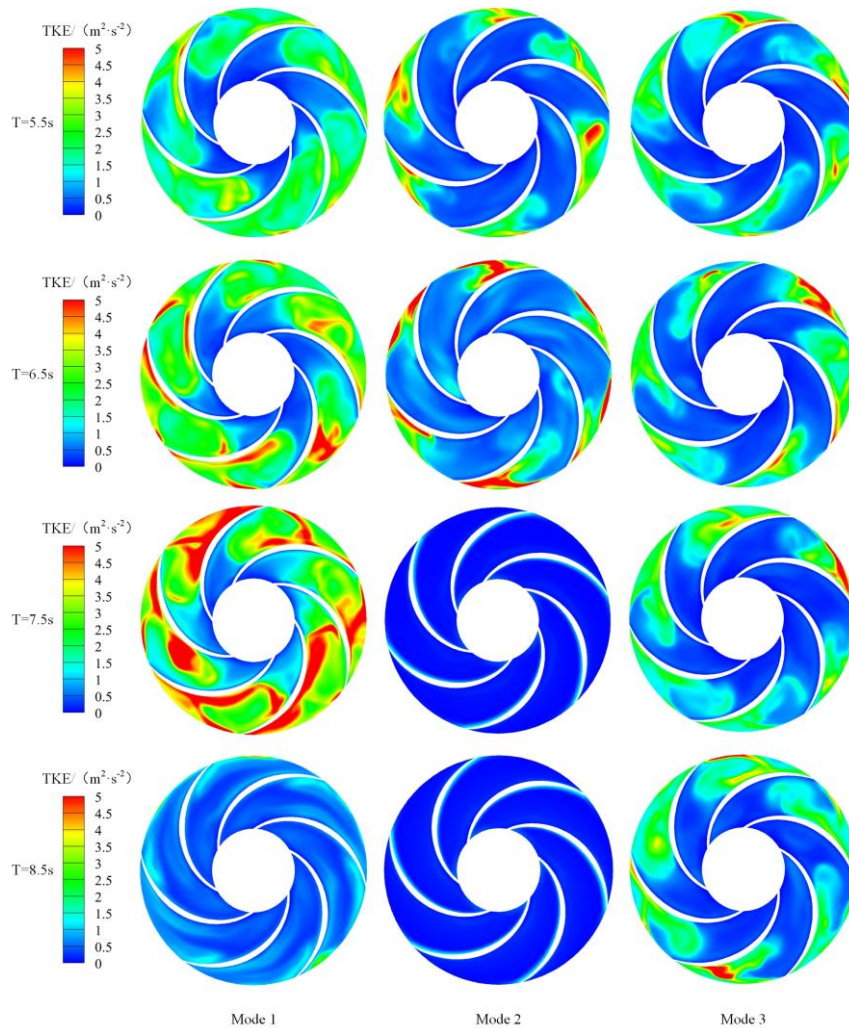


**Fig. 11 Turbulent kinetic energy distribution at the mid-section of the impeller under different pump starting modes**

turbulent kinetic energy distribution. This distribution pattern of the turbulent kinetic energy in Mode 2 also contributed to the reduction in the peak value of the external pressure characteristic curve.

### 3.6 Pressure Load Distribution on the Blades under the Three Pump Start-up Modes

During pump start-up, the pressure load on each blade is defined by the variation in pressure on the pressure side and suction side along the blade length at different moments. Analyzing the blade loads at different moments under various pump start-up modes helps to better understand the fluid flow within the impeller and assess whether impact phenomena occur during the start-up process. Figure 12 shows the pressure load distribution along the midstreamline of the pressure and suction surfaces of the blade when the pump speed reached the rated speed ( $T = 7.5$  s,  $T = 8.5$  s). The x-axis represents the dimensionless length from the blade inlet to the blade outlet;  $x = 0$  corresponds to the blade inlet,  $x = 1.0$  corresponds to the blade outlet, and the y-axis represents the static pressure of the blades.

The static pressure distribution across the blades of the impeller in the figure is generally consistent, and the

static pressure values on the suction surfaces of all six blades were lower than those on the pressure surfaces. The blade load exhibited an increasing trend from the blade inlet to the outlet, followed by a decrease.

By comparing the figures, it can be observed that the blade load distribution curve shows a sharp increase at the x-axis coordinate of 0.75, which corresponds to three-quarters of the blade length, and this increase persists until the blade outlet. In Mode 2, the static pressure distribution curves on the pressure and suction surfaces of the blades are essentially overlapping and continuous. The reason for this phenomenon is as follows: In Mode 2, at 7.5 and 8.5 s, the pump has reached the rated speed and is operating under design conditions, the flow inside the impeller is stable, and the fluid flows uniformly through the impeller passages, resulting in an even load distribution on both the pressure and suction surfaces of the blades. At 7.5 s in Mode 1, when the valve initially opens, the flow inside the pump is complex and remains in a low-flow state, causing uneven fluid development in the impeller passages. The significant change in fluid flow at the junction between the blade exit and volute results in a sudden increase in load near the blade exit. In Mode 3, the pump speed has not yet reached the rated value, resulting in a low flow rate within

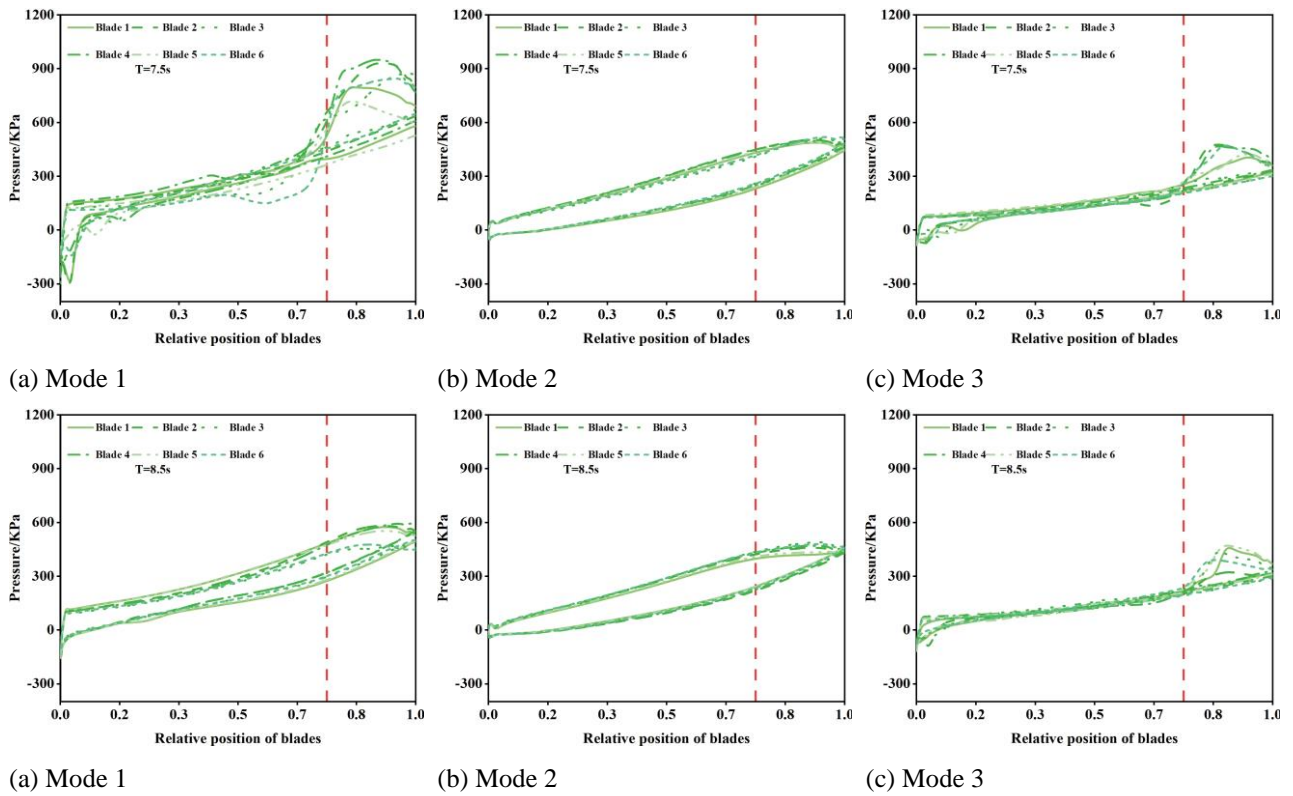


**Fig. 12 Load distribution along the midstreamline of the blades under different pump start-up modes**

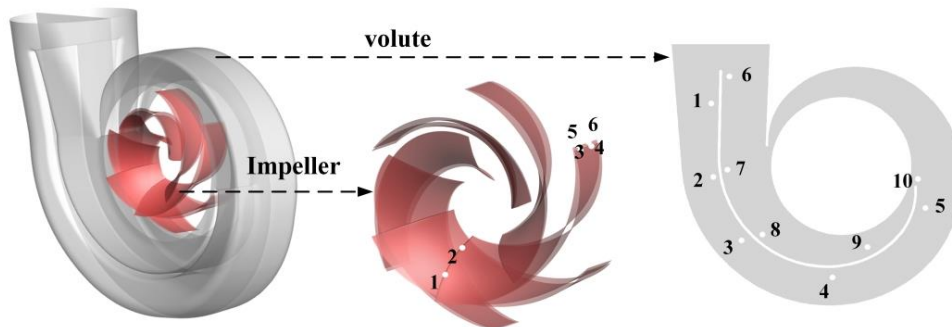


**Fig. 13 Monitoring points at the impeller and volute**

the impeller and causing uneven fluid forces on the blades. In contrast, the load distribution pattern of the blades in Mode 2 during start-up is more pronounced, demonstrating a clear trend after the start-up process is completed. This load distribution pattern clearly indicates that, in Mode 2, when the pump reaches its rated speed, the flow field remains relatively stable, resulting in a uniform pressure distribution across the blade surfaces, which is consistent with the velocity and pressure contour distributions.

### 3.7 Pressure Fluctuation Phenomena under Three Different Starting Modes

Rapid changes in various parameters during the pump start-up process lead to complex pressure fluctuations, which can affect the normal operation of the pump. Therefore, studying the pressure fluctuations at the impeller and volute positions under the three pump start-up modes provides a deeper understanding of the transient

start-up process. In this study, two monitoring points were set at the impeller blade leading edge, working surface trailing edge, and back surface trailing edge to monitor the pressure fluctuations during the pump start-up process. In addition, five monitoring points were set at the inner and outer volute plates to monitor the pressure fluctuations within the volute during the start-up process. The layout of the monitoring points is shown in Fig. 13.

During the calculation, the rotational speed of the centrifugal pump was 375 rpm, and the number of blades was six; therefore, the shaft frequency of the pump during operation was 6.25 Hz, and the blade-passing frequency was 37.5 Hz. To visually represent the pressure pulsation characteristics corresponding to the start-up mode under specific operating conditions, the dimensionless pressure pulsation coefficient,  $C_p$ , was introduced for data analysis. The specific equation is as follows:

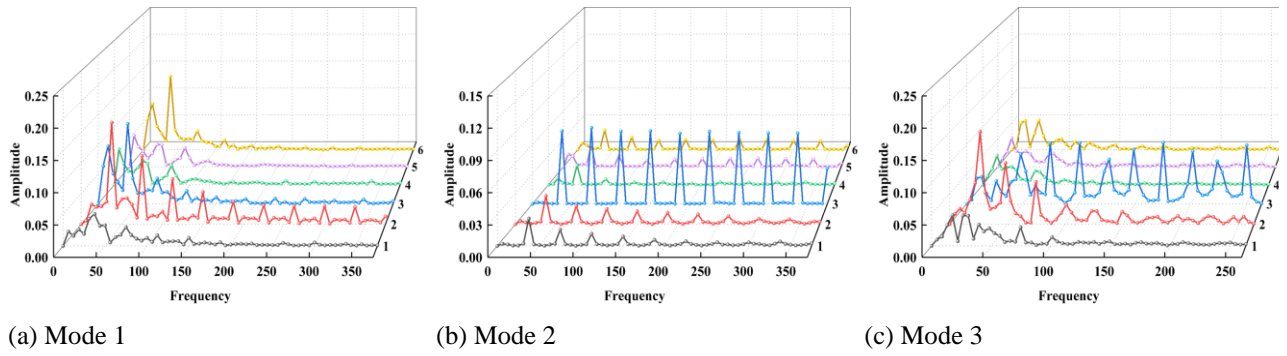


**Fig. 14 Pressure pulsation frequency domain diagram for the impeller monitoring points**

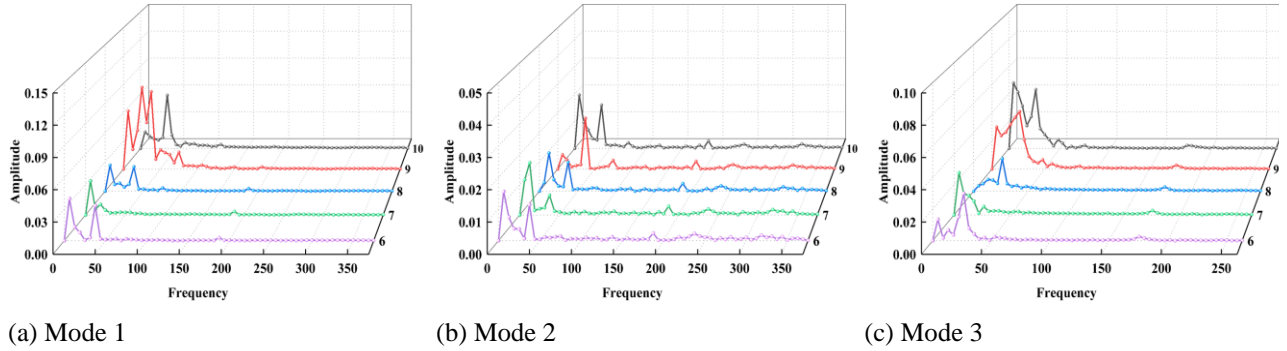


**Fig. 15 Pressure pulsation frequency domain diagram for monitoring points on the inner partition of the volute**

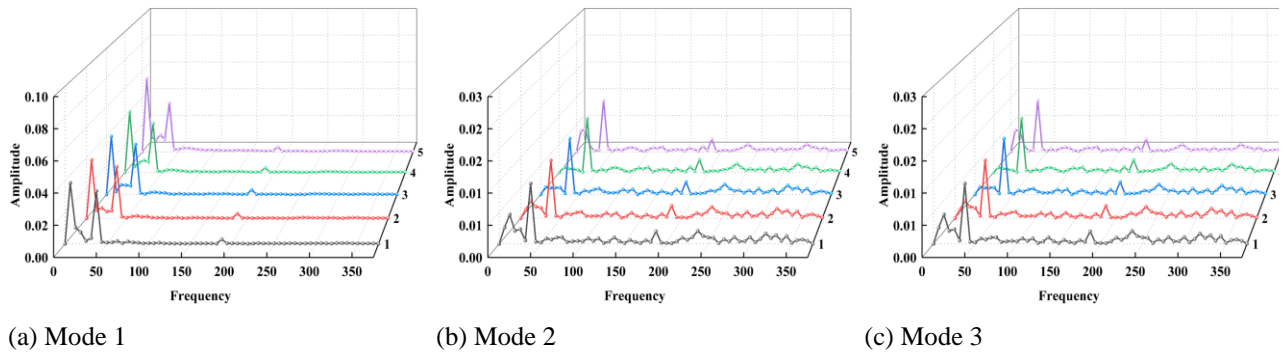


**Fig. 16 Pressure pulsation frequency domain diagram for monitoring points on the outer partition of the volute**

$$C_p = \frac{P - \bar{P}}{0.5\rho u^2} \quad (9)$$

In the equation,  $p$  represents the instantaneous pressure at each monitoring point during the start-up process, Pa;  $\bar{p}$  represents the time-averaged pressure at each monitoring point, Pa;  $u$  represents the circumferential velocity at the impeller outlet, m/s, and is calculated using the following equation:

$$u = \frac{\pi D n_d}{60} \quad (10)$$

where  $D$  is the outer diameter of the impeller, 1.817 m, and  $n_d$  is the rated rotational speed of the impeller, 375 rpm.

The frequency domain diagram for the pressure pulsation monitoring point  $C_p$  under each start-up mode, obtained through a fast Fourier transform (FFT) at 7.5 s,

is shown below. Figure 14 shows a pressure pulsation frequency domain diagram of the monitoring points on the impeller. Figure 15 shows a pressure pulsation frequency domain diagram of the monitoring points on the inner partition of the volute. Figure 16 shows a pressure pulsation frequency domain diagram of the monitoring points on the outer partition of the volute.

In Fig. 14, under the three different pump start-up modes, the frequency domain distribution of the impeller position monitoring points in start-up Mode 2 is the most uniform. In Fig. 14a, the maximum pressure pulsation amplitude under Mode 1 is located at monitoring point 2, with a value of 0.1653. In Fig. 14b, the maximum pressure pulsation amplitude under Mode 2 is found at monitoring point 3, measuring 0.0733. In Fig. 14c, the maximum pressure pulsation amplitude under Mode 3 is observed at monitoring point 2, with a value of 0.0402. The amplitude values at the monitoring points inside the impeller are the highest in Mode 1 and gradually decrease in Modes 2 and

**Table 4 Distribution of fundamental frequencies at maximum pressure pulsation amplitude points**

Pump start-up mode	Monitoring area	Blade passing frequency	Shaft frequency	Maximum amplitude point	Fundamental frequency
Mode 1	Impeller	37.5	6.25	2	37.5
Mode 2		37.5	6.25	3	37.5
Mode 3		37.5	6.25	2	37.5
Mode 1	Inner partition of the volute	37.5	6.25	9	6.25
Mode 2		37.5	6.25	10	6.25
Mode 3		37.5	6.25	10	6.25
Mode 1	Outer partition of the volute	37.5	6.25	5	6.25
Mode 2		37.5	6.25	4	37.5
Mode 3		37.5	6.25	5	6.25

3, which is consistent with the variation in external characteristics. The fundamental frequency at the impeller inlet monitoring points 1 and 2 in all three start-up modes corresponds to the blade passing frequency, indicating that the inlet position of the blades is significantly influenced by the rotational frequency during the start-up process.

In Fig. 15, the pressure pulsation frequency domain distribution at the inner partition of the volute is more uniform compared with that at the impeller position under all three start-up modes, but the pressure pulsation amplitude increases across the three modes. In Fig. 15a, the maximum pressure pulsation amplitude under Mode 1 is located at monitoring point 9, with an amplitude value of 0.0614. In Fig. 15b, the maximum pressure pulsation amplitude under Mode 2 is found at monitoring point 10, measuring 0.0158. In Fig. 15c, the maximum pressure pulsation amplitude under Mode 3 is also observed at monitoring point 10, with a value of 0.048. Among the three modes, the amplitude at the monitoring point in Mode 2 is the smallest, indicating that the pressure pulsation phenomenon within the inner partition of the volute is relatively subdued in this mode, which is consistent with the variation in the external characteristics. At the same time, the large pressure pulsation amplitude at positions 9 and 10 indicates a strong rotor–stator interaction between the inner partition of the volute and the impeller during the start-up process. This results in an irregular influence on the monitoring points of the inner partition caused by both the rotational frequency and the blade passing frequency of the impeller.

In Fig. 16, the pressure pulsation frequency domain diagram for the monitoring points on the outer partition of the volute shows a more regular distribution compared with that at the monitoring points located at the impeller and inner partition of the volute, with the primary and secondary frequencies clearly distinguishable. In Fig. 16a, the maximum pressure pulsation amplitude under Mode 1 is located at monitoring point 5, with an amplitude value of 0.054. In Fig. 16b, the maximum pressure pulsation amplitude under Mode 2 is found at monitoring point 4, measuring 0.0115. In Fig. 16c, the maximum pressure pulsation amplitude under Mode 3 is observed at monitoring point 5, with a value of 0.0375. In Mode 2, the pressure pulsation amplitude at the outer partition monitoring points is the smallest, which is consistent with the variation in the external characteristics.

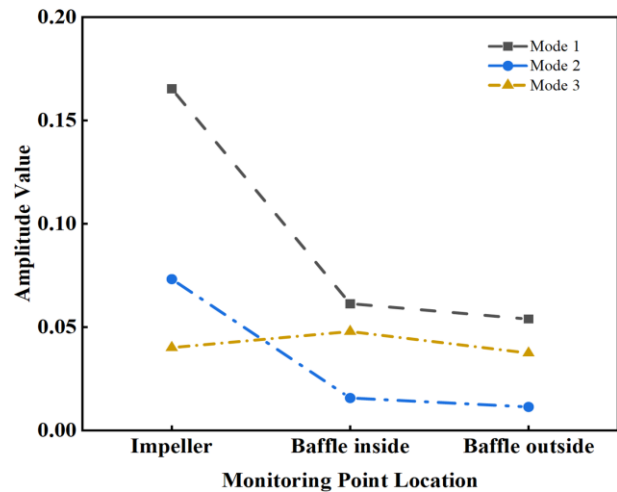


**Fig. 17 Variation of maximum amplitude**

Table 4 lists the distributions of the fundamental frequencies at the maximum pressure pulsation amplitude points for the three start-up modes. From the table, it can be concluded that whether the pump speed has increased to the rated speed before valve opening does not affect the fundamental frequency at the monitoring point with the maximum amplitude on the impeller, which is consistently the first harmonic of the blade passing frequency (1x blade passing frequency). It also does not affect the fundamental frequency at the monitoring point with the maximum amplitude on the inner partition of the volute, which is consistently the first harmonic of the shaft frequency (1x shaft frequency). When the valve is opened early, as the pump reaches 0.7 times the rated speed, the fundamental frequency at the maximum pressure pulsation point on the outer partition is the blade passing frequency.

Figure 17 shows the variations in the maximum amplitude values of the pressure pulsations at the impeller, inner partition of the volute, and outer partition positions in the pressure pulsation frequency domain diagram. Under the three pump start-up modes, the pressure pulsation amplitude values were the smallest in Mode 2 for both the impeller and the inner and outer partitions of the volute. In the impeller, the pressure pulsation amplitude values in Modes 2 and 3 decreased by 55.56% and 75.68%, respectively, compared with that in Mode 1. In the inner partition of the volute, the pressure pulsation amplitude values in Modes 2 and 3 decreased by 74.26%

and 21.82%, respectively, compared with that in Mode 1. In the outer partition of the volute, the pressure pulsation amplitude values in Modes 2 and 3 decreased by 78.70% and 30.56%, respectively, compared with that in Mode 1. This indicates that the Mode 2 start-up method can effectively alleviate pressure fluctuations within the pump, which is consistent with the observation that this mode significantly reduces the pressure peak phenomena during the start-up process across all three start-up modes.

#### 4. CONCLUSION

This study employs a combined one- and three-dimensional simulation approach to calculate and simulate the changes in the external and internal flow characteristics of a large centrifugal pump system during linear and staged start-up processes. The main conclusions are as follows.

Regarding valve and pump coordination in large centrifugal pump systems: The length of the valve opening time affects both the magnitude of the pressure peak and the duration of the pressure peak under both linear and staged start-up modes. For a linear start-up, as the valve opening time increases, the pump outlet pressure peak remains unchanged, whereas the duration of the pump outlet pressure peak increases. For a staged start-up, as the valve opening time increases, the pressure peak becomes larger, and the duration of the pump outlet pressure peak also increases.

Regarding the external characteristics of the large centrifugal pump system: In large centrifugal pump systems, the staged start-up method can effectively reduce the instantaneous pressure peak at the pump outlet compared with the linear start-up method. Specifically, during the staged start-up, the pump outlet pressure peak is significantly reduced, from 77.71 m in the linear start-up to 59.11 and 59.04 m.

Regarding the internal flow field and pressure fluctuations of the large centrifugal pump system: In large centrifugal pump systems, the staged start-up method can effectively reduce the severe pressure fluctuations, sudden changes in blade load, and fluid turbulence during start-up. In the staged start-up mode, where the valve is opened in advance when the pump speed reaches 0.7 times the rated speed, compared with the pump–valve coordination mode, where the valve is opened when the pump reaches the rated speed directly, the maximum amplitude of the pressure fluctuation at the monitoring points located at the impeller, volute internal baffles, and volute external baffles decreases by 55.56%, 74.26%, and 78.70%, respectively. This significantly alleviates the pressure pulsation within the pump, thereby ensuring smoothness and stability of the start-up process.

#### ACKNOWLEDGEMENTS

This research was funded by the National Science Foundation for Distinguished Young Scholars of China (52009051) and Gansu Province Natural Science Foundation of China (23JRRA800).

#### CONFLICT OF INTEREST

The authors declare no conflicts of interest.

#### AUTHORS CONTRIBUTION

**Fu You:** Methodology, writing – review and editing;  
**Qi Mu Lan:** Data Curation, software validation, writing – original draft preparation.

#### References

- Desheng, S. Z., Qiang, Z., & Qi, G. (2022). Experimental and numerical investigation on the transient cavitating flows in a mixed flow pump with different number of blades at start up. *Journal of Fluids Engineering*, 144(5), 051204. <https://doi.org/10.1115/1.4052863>
- Ding, H., Ge, F., & Wang, K. (2023). Influence of blade trailing-edge filing on the transient characteristics of the centrifugal pump during start up. *Processes*, 11(8), 2420. <https://doi.org/10.3390/pr11082420>
- Feng, J. J., Zhang, Y., & Zhu, G. J. (2020). Transition process characteristics of centrifugal pump with power-off based on entropy production theory. *Transactions of the Chinese Society of Agricultural Engineering*, 36(4), 10-17. <https://doi.org/10.11975/j.issn.10026819.2020.04.002>
- Fu, X., Li, D., Wang, H., Li, Z., Zhao, Q., & Wei, X. (2021). One- and three-dimensional coupling flow simulations of pumped-storage power stations with complex long-distance water conveyance pipeline system. *Journal of Cleaner Production*, 315, 128228. <https://doi.org/10.1016/j.jclepro.2021.128228>
- Gu, M. X. (2021). Review of the full characteristic curves of pumps in long-distance water transport systems. *Innovation Science and Technology*, (17), 30-31. <https://doi.org/10.1016/j.enconman.2018.07.091>
- Kan, K., Zheng, Y., Chen, H. X., Zhou, D. Q., Dai, J., Binama, M., & Yu, A. (2020). Numerical simulation of transient flow in a shaft extension tubular pump unit during runaway process caused by power failure. *Renewable Energy*, 154, 1153-1164. <https://doi.org/10.1016/j.renene.2020.03.057>
- Li, Q., Ma, X., & Wu, P. (2020). Study on the transient characteristics of the centrifugal pump during the start up period with assisted valve. *Processes*, 8(10), 1241. <https://doi.org/10.3390/pr8101241>
- Li, Q., Zhang, R., & Kang, C. (2022). Transient characteristics during start-up of dual pumps in the prefabricated pumping station. *AQUA—Water Infrastructure, Ecosystems and Society*, 71(10), 1229-1240. <https://doi.org/10.2166/aqua.2022.234>
- Li, W., Lu, D. L., & Ma, L. (2021a). Experimental study on pressure vibration characteristics of mixed-flow pump during start-up. *Trans. Chin. Soc. Agric. Eng.*, 37, 44-50. <https://doi.org/10.11975/j.issn.1002-6819.2021.01.006>
- Li, W., Ma, L., & Shi, W. (2021b). Numerical simulation

- of inlet flow characteristics of mixed flow pumps during start-up. *China Mechanical Engineering*, 32(06): 666. <https://doi.org/10.3969/j.issn.1004-132X.2021.06.005>
- Lin, T., Li, X., Zhu, Z. (2021). Application of enstrophy dissipation to analyze energy loss in a centrifugal pump as turbine. *Renewable Energy*, 163, 41-55. <https://doi.org/10.1016/j.renene.2020.08.109>
- Liu, B. X., Lu, J. L., Feng, J. J. (2024a). Influence of valve plate wake on the performance of centrifugal pump. *Transactions of the Chinese Society of Agricultural Engineering (Transactions of the CSAE)*, 40(2), 217-227. <https://doi.org/10.11975/j.issn.1002-6819.202308053>
- Liu, S., Ma, A., & Zhao, X. (2024b). Characteristic analysis of pressure fluctuation of the super large flow and high-power centrifugal pump during transient processes of the start-up and shutdown. *Journal of Physics: Conference Series*, 2752(1), 012133. <https://doi.org/10.1088/1742-6596/2752/1/012133>
- Lu, Y. P., Ma, C., Tan, L., & Han, Y. (2022). Theoretical model of transient mixed-flow pump start-up. *Journal of Tsinghua University (Science and Technology)*, 62(12), 1938-1944. <https://doi.org/10.16511/j.cnki.qhdxxb.2022.26.007>
- Shi, L., Zhang, J., & Yu, X. D. (2023). Study on reducing height of surge tank in long-distance and multi-branch water conveyance system. *Journal of Huazhong University of Science and Technology (Natural Science Edition)*, 51(08), 67-73. <https://doi.org/10.13245/j.hust.230812>
- Tanaka, T., Toyomoto, T., & Nasu, K. (2021). Transient characteristics of a centrifugal pump at rapid start up. *Journal of Physics. Conference Series*, 1909(1), 012032. <https://doi.org/10.1088/1755-1315/240/5/052016>
- Tang, Z., Zhu, G., & Feng, J. (2023). Influence of pump start-up mode on the stability of mixed-flow pumps. *Journal of Mechanical Science and Technology*, 37(6), 2949-2958. <https://doi.org/10.1007/s12206-023-0521-7>
- Wang, L., Li, M., & Wang, F. J. (2017). Study on three-dimensional internal characteristics method of Suter curves for double-suction centrifugal pump. *Journal of Hydraulic Engineering*, 48, 113-122. <https://doi.org/10.13243/j.cnki.slxb.20160667>
- Wang, X. H., Jiang, H. Z., Miao, S. C., Bai, X. B., & Qi, B. (2024). Analysis of Energy Dissipation Mechanism of Multistage Hydraulic Turbine Based on Entropy Production Theory. *Transactions of the Chinese Society for Agricultural Machinery*, 55(3), 162-172. <https://doi:10.6041/i.issn.1000-298.2024.03.016>
- Xia, Y., Mao, J., & Li, G. (2024). Analysis of internal flow characteristics of a multistage pump during start-up. *Journal of Physics: Conference Series*, 2707(1), 012025. <https://doi.org/10.1088/1742-6596/2707/1/012025>
- Xu, H., Gong, Y., Cao, C. J., Chen, H. X., & Feng, J. G. (2021). 3D start-up transition process of full flow system for shaft-extension tubular pump station. *Transactions of the Chinese Society for Agricultural Machinery*, 52(4), 143-151. <https://doi.org/10.6041/j.issn.1000-1298.2021.04.015>
- Yun, L., Bin, L., & Jie, F. (2020). Research on the transient hydraulic characteristics of multistage centrifugal pump during start-up process. *Frontiers in Energy Research*, 8, 76. <https://doi.org/10.3389/fenrg.2020.00076>
- Zhang, F. Y., Lu, H., Chen, T. R., Wu, Q., Huang, B., Wang, G. Y. (2021). Transient characteristics of start-up process of an axial flow water-jet propeller. *Acta Armamentarii*, 42(8), 1592-1603. <https://doi.org/10.3969/j.issn.1000-1093.2021.08.003>
- Zhang, H., Sun, J., & Dong, W. (2024). Numerical analysis of the transient characteristics of internal flow in the acceleration process of variable speed regulation of a centrifugal pump. *Journal of Physics*, 2752(1), 012097. <https://doi.org/10.1088/1742-6596/2752/1/012097>
- Zhang, Y. L., Zhang, K. Y., & Li, J. F. (2022). Effect of rotational speed and flowrate on the start up characteristics of a pumps as turbine. *Measurement and Control*, 55(9-10): 1043-1056. <https://doi.org/10.1177/00202940221098052>